Nanoscale Advances

ROYAL SOCIETY OF CHEMISTRY

PAPER

View Article Online
View Journal | View Issue

Cite this: *Nanoscale Adv.*, 2023, **5**, 4782

A bacterial cellulose-based $LiSrVO_4:Eu^{3+}$ nanosensor platform for smartphone sensing of levodopa and dopamine: point-of-care diagnosis of Parkinson's disease†

Mohammad Mahdavi, Hamid Emadi * and Seyed Reza Nabavi

Among the catecholamines, dopamine (DA) is essential in regulating multiple aspects of the central nervous system. The level of dopamine in the brain correlates with neurological diseases such as Parkinson's disease (PD). However, dopamine is unable to cross the blood–brain barrier (BBB). Therefore, levodopa (LD) is used to restore normal dopamine levels in the brain by crossing the BBB. Thus, the control of LD and DA levels is critical for PD diagnosis. For this purpose, $LiSr_{0.0985}VO_4:0.015Eu^{3+}$ (LSV:0.015Eu^{3+}) nanoplates were synthesized by the microwave-assisted co-precipitation method, and have been employed as an optical sensor for the sensitive and selective detection of catecholamines. The synthesized LSV:0.015Eu^{3+} nanoplates emitted red fluorescence with a high quantum yield (QY) of 48%. By increasing the LD and DA concentrations, the fluorescence intensity of LSV:0.015Eu^{3+} nanoplates gradually decreased. Under optimal conditions, the linear dynamic ranges were 1–40 μM (R^2 = 0.9972) and 2–50 μM (R^2 = 0.9976), and the detection limits (LOD) were 279 nM, and 390 nM for LD and DA, respectively. Herein, an instrument-free, rapid quantification visual assay was developed using a paper-based analytical device (PAD) with LSV:0.015Eu^{3+} fixed on the bacterial cellulose nanopaper (LEBN) to determine LD and DA concentrations with ease of operation and low cost. A smartphone was coupled with the PAD device to quantitatively analyze the fluorescence intensity changes of LSV:0.015Eu^{3+} using the color recognizer application (APP). In addition, the LSV:0.015Eu^{3+} nanosensor showed acceptable repeatability and was used to analyze real human urine, blood serum, and tap water samples with a recovery of 96–107%.

Received 5th May 2023
Accepted 31st July 2023

DOI: 10.1039/d3na00297g

rsc.li/nanoscale-advances

Introduction

Catecholamines (CAs) are a class of neurotransmitters characterized by amines and catechols that act as hormones in the peripheral endocrine and central nervous systems. They are synthesized in nerves at the site of their release, both on the terminals and in cellular bodies. CAs exist in low concentrations within the brain as amino acid neurotransmitters, including glutamate and γ-aminobutyric acid. Their function in regulating multiple aspects of the central nervous system makes them important therapeutic targets. Among the various catecholamines, dopamine (DA) is a fascinating neurotransmitter for chemists and neuroscientists, and is derived from the decarboxylation of 3,4-dihydroxyphenylalanine (L-DOPA (LD)).[1] DA is a neurotransmitter that plays several roles such as controlling mood, regulating movement, making decisions, sleeping, and dreaming.[2] In addition, changes in the amount of DA are frequently linked to neurological illnesses, including Parkinson's disease (PD).[3] Dopamine, as a neurotransmitter, can transmit electrical signals between neurons and the central nervous system. Low dopamine levels can cause symptoms and disruptions to the dopaminergic pathways in the brain, specifically the mesolimbic and substantia nigra routes. In patients with PD, these pathways are no longer connected, leading to decreased dopamine levels.[4] PD causes movement disorders along with cognitive manifestations, leaving the patient neurologically impaired. Its clinical manifestations include static tremors, postural problems, and stiffness, all of which profoundly affect a patient's quality of life.[5] Research has shown that PD is mainly associated with low levels of dopamine in the

Department of Applied Chemistry, Faculty of Chemistry, University of Mazandaran, Babolsar, Iran. E-mail: h.emadi@umz.ac.ir; m.mahdavi10@umail.umz.ac.ir; srnabavi@umz.ac.ir

† Electronic supplementary information (ESI) available: EDX spectra and elemental mapping of LSV:0.015Eu^{3+}, stability of LSV:0.015Eu^{3+} nanoplates at different storage and UV irradiation times, DRS spectra of LSV and LSV:0.015Eu^{3+}, information about optimization with Design Expert software, FESEM images of bacterial cellulose nanopaper and bacterial cellulose nanopaper immersed in LSV:0.015Eu^{3+} solution, calculation of τ_{av} for fluorescence lifetime decay, comparison of LOD and real sample data. See DOI: https://doi.org/10.1039/d3na00297g

brain.[6] LD is often prescribed as the major precursor of dopamine. Although dopamine cannot cross the BBB, LD can enter the brain without being metabolized and then converted into DA through an enzymatic reaction catalyzed by dopadecarboxylase to restore normal dopamine levels in the brain.[7] Consequently, it improves Parkinson's symptoms by increasing dopamine levels in the brain.[8] LD is the most commonly prescribed drug for PD in the clinical setting. Moreover, excessive levodopa accumulation may cause movement disorders, hypotension, arrhythmia, nausea, and confusion. Therefore, determining and controlling LD and DA concentrations are necessary to improve PD treatment.[8,9] High-performance liquid chromatography (HPLC),[10] capillary electrophoresis (CE),[11] chemiluminescence,[12] electrochemical detections,[13] and fluorescence-based methods[14] have been developed to determine LD and DA concentrations. These methods have many shortcomings, such as low sensitivity, long detection periods, and the need for expensive tools and professional technicians.[15] Therefore, it is crucial to develop rapid, low-cost, sensitive, and selective techniques for determining LD and DA concentrations. Recently, fluorescence-based sensors have been considered satisfactory owing to their excellent characteristics of sample preparation, simplicity, and real-time monitoring.[16] Fluorescence detection uses various probes, which most of them consist of fluorescent organic dyes capable of detecting molecules or ions.[17] Organic dyes have numerous disadvantages, such as photobleaching, poor chemical stability, a wide range of emissions, and difficulty conjugating with ligands targeting.[18] Accordingly, luminescent nanomaterials have been developed to replace conventional fluorescent organic dyes.[17] Various nanomaterials have luminescence properties, such as some metals,[19] quantum dots,[9] silicon nanoparticles,[20] and nanophosphors.[21] Rare Earth (RE) nanophosphors have significant benefits because of their low toxicity, photostability, large Stokes shifts, sharp emission bands, and high luminescence quantum yields.[22] These nanomaterials typically comprise inorganic crystalline matrices doped with luminescent lanthanide cations (Ln^{3+}). A crucial issue for nanophosphors is that the host lattice must be physically and chemically stable. Owing to their high luminescence efficiency and chemical permanence, vanadate-based compounds have attracted attention for use in conventional luminescent host lattices.[23,24] There is a correlation between the colors given off by luminescent compounds and their structural properties, as longer V–O distances in the $(VO_4)^{3-}$ tetrahedra in the crystal structures are associated with longer photoluminescence wavelengths.[25] Furthermore, an ionic complex group $(VO_4)^{3-}$, consisting of a vanadium ion coordinated to four O^{2-} ions in a tetrahedral symmetry, was found to be an effective luminescent center.[26] Vanadate compounds doped with rare-earth ions (Eu^{3+}, Ho^{3+}, Tm^{3+}, Nd^{3+}, Er^{3+}, Pr^{3+}, and Yb^{3+}) as phosphors emit various colors of light because of their high luminescence quantum yields.[27] These ions have narrow and parity-forbidden intra-configurational 4fn ↔ 4fn transitions, which cause the emission of different light colors.[28]

Vanadate compounds doped with lanthanides have been used as probes in optical sensors because of their high fluorescence properties.[22] Zeng *et al.* used $Y(V_{0.2}P_{0.8}O_4):Eu^{3+}$ as turn-off luminescence probes for the detection of Cr(III).[29] Also, Abbasi-Moayed *et al.* synthesized $NaYF_4$:Yb/Er/Tm as fluorescent probes for the detection of neurotransmitters such as DA and LD.[14] As a result, nanophosphors based on vanadate compounds doped with lanthanides can be used to fabricate fluorescent probes.[27,30]

Recently, bacterial cellulose nanopaper, in combination with nanophosphors, has been widely used as a low-cost, sensitive, and visual alternative to conventional analytical tools.[31,32] Bacterial cellulose nanopaper can be considered as an appropriate substrate for determining LD and DA concentrations because of its low cost, flexibility, biocompatibility, eco-friendly, high surface area, high porosity, water absorbance, and optical transparency.[33] Despite some progress in the visual analysis of objects using paper-based sensors, it remains challenging to achieve satisfactory sensitivity and accuracy because our naked eyes are not capable of detecting subtle color changes. As an alternative solution, smartphones are connected to paper-based sensors that provide portability, high-quality imaging, and result analysis *via* color recognition applications (APP).[34]

In the current study, $LiSrVO_4:Eu^{3+}$ ($LSV:Eu^{3+}$) nanostructure was synthesized as a luminescent material by microwave-assisted co-precipitation method. Microwave-assisted synthesis provides rapid and homogeneous nucleation which leads to rapid particle growth and narrow size distribution in the final product.[35] Microwave interactions with reactants at the molecular level and the conversion of electromagnetic energy into heat have a significant effect on the formation of nanostructures.[36] Microwave-assisted synthesis methodologies are incredibly versatile and reduce the energy consumption and reaction time for synthesizing inorganic luminescent materials. Additionally, microwave irradiation is more efficient than conventional heating, leading to an increased reaction rate owing to ion diffusion facilitated by the electromagnetic field of microwaves.[37] A rapid heating rate can induce the formation of structural defects, which allows for the high storage capacity of the phosphors.[38] The synthesized products were used to determine LD and DA concentrations using a smartphone. A smartphone with an android operating system connected to a paper-based analytical device (PAD) was used to determine the LD and DA concentrations in the presence of a bacterial cellulose nanopaper coated with $LSV:Eu^{3+}$.

Experimental section

Reagents and chemicals

Strontium nitrate ($Sr(NO_3)_2$) anhydrous, europium nitrate hexahydrate ($Eu(NO_3)_3 \cdot 6H_2O$), lithium nitrate ($LiNO_3$) and ammonium metavanadate (NH_4VO_3) were purchased from Merck (Darmstadt, Germany). Nitric acid (HNO_3), levodopa (LD), dopamine (DA), sodium chloride (NaCl), L-cysteine (L-Cys), calcium chloride ($CaCl_2$), ascorbic acid (AA), rhodamine B, glucose, urea ($CO(NH_2)_2$), glutamine (Glu), and aspirin were bought from Sigma Aldrich (St. Louis, MO, USA). The chemicals used in the experiment were of AR grade and were not purified further. The solutions were prepared using deionized (DI) water with a conductivity of 18.25 MΩ.

Characterization

Structural phase-purity characterization of Eu^{3+} doped LSV phosphors was performed using X-ray Powder Diffraction (XRD) patterns. The XRD patterns were recorded in the 2θ range of 10°–70° using a Philips diffractometer (1.5406 Å). The Thermo Avatar spectrophotometer was used to analyze the Fourier-transform infrared (FTIR) spectra of the synthesized samples. A KBr pellet technique was used for this purpose. The morphology and the microstructure of the prepared LSV:0.015Eu^{3+} nanoplates were imaged by field emission scanning electron microscopy (FESEM, MIRA 3-XMU) and transmission electron microscopy (TEM, Philips EM 208S). The elemental analysis images of the samples were obtained by using energy-dispersive X-ray spectroscopy (EDX, TESCAN MIRA). The elemental composition and contents were confirmed by X-ray photoelectron spectra (XPS, SPESS UHV analysis system). Diffuse reflectance spectra (DRS) were obtained in the range from 200 to 800 nm by a UV-Vis NIR (SHIMADZU-2600) spectrophotometer. Fluorescence and ultraviolet-visible (UV-Vis) spectra were collected from a Jasco V-750 FL spectrometer. Fluorescence lifetime was measured using a steady state (Edinburgh instruments ex-demo equipment f900 spectrophotometer).

Preparation of $LiSr_{(1-x)}VO_4:xEu^{3+}$

The $LiSr_{(1-x)}VO_4:xEu^{3+}$ (0.00, 0.0085, 0.001, 0.0115, 0.0125, 0.0135, 0.015, 0.0165, and 0.018 mol) samples were synthesized by a microwave-assisted co-precipitation method. In a typical synthesis, stoichiometric amounts of the $LiNO_3$, $Sr(NO_3)_2$, and $EuCl_3 \cdot 6H_2O$ were added to 10 ml deionized (DI) water, followed by adding 4 ml of 0.1 M HNO_3 dropwisely. The reaction mixture was heated at 80 °C under stirring for 35 minutes until the paste was completely dissolved. Then 10 ml of 0.05 M solution of NH_4VO_3 was added dropwisely to the above-mentioned solution. Subsequently, the final solution was transferred to the microwave oven (MILESTONE MICROSYNTH) and irradiated at a power of 325 W for 25 minutes, and then a reddish precipitate was obtained. The obtained precipitate was dried and calcined at 900 °C for 3 h to get a white crystalline powder of $LiSr_{(1-x)}VO_4:xEu^{3+}$. In addition, the optimal concentration of Eu^{3+} ions, which had the highest fluorescence intensity, was 0.015 mol of Eu^{3+}. The synthesis procedure for $LiSr_{(1-x)}VO_4:xEu^{3+}$ is summarized in Scheme 1.

Detection assays for LD

Different concentrations (0, 1, 2, 5, 10, 20, 30, 40, 75, 100, 150, 200, 500, 750, and 1000 μM) of LD solution were prepared. Then 1.5 ml of LD solution with different concentrations was added to 1.5 ml of the LSV:0.015Eu^{3+} solution. The mixture was then incubated for 5 min under normal conditions at room temperature. In addition, the volumes of the LD and LSV:0.015Eu^{3+} solutions were constant throughout the experiment. Fluorescence measurements were conducted under optimal conditions at ambient temperature at an excitation wavelength of 330 nm. The fluorescence intensity was averaged over three measurements.

Detection assays for DA

Various concentrations (0, 2, 5, 10, 20, 30, 40, 75, 100, 150, 200, 500, 750, and 1000 μM) of DA solution were prepared. Then 1.5 ml of DA solution with different concentrations was added to 1.5 ml of LSV:0.015Eu^{3+} solution. The mixture was incubated for 7 minutes at room temperature under optimal conditions. The added volumes of the DA and LSV:0.015Eu^{3+} in all experiments were constant. Therefore, the fluorescence emission spectrum was gathered at the excitation wavelength of 330 nm. Fluorescence measurements were made at ambient temperature under optimal conditions and averaged over three measurements.

Preparation of test paper

To fabricate the LEBN (LSV:0.015Eu^{3+} bacterial cellulose nanopaper) sensing platform, bacterial cellulose nanopaper was cut to a diameter of 1 cm and immersed in a Petri dish containing

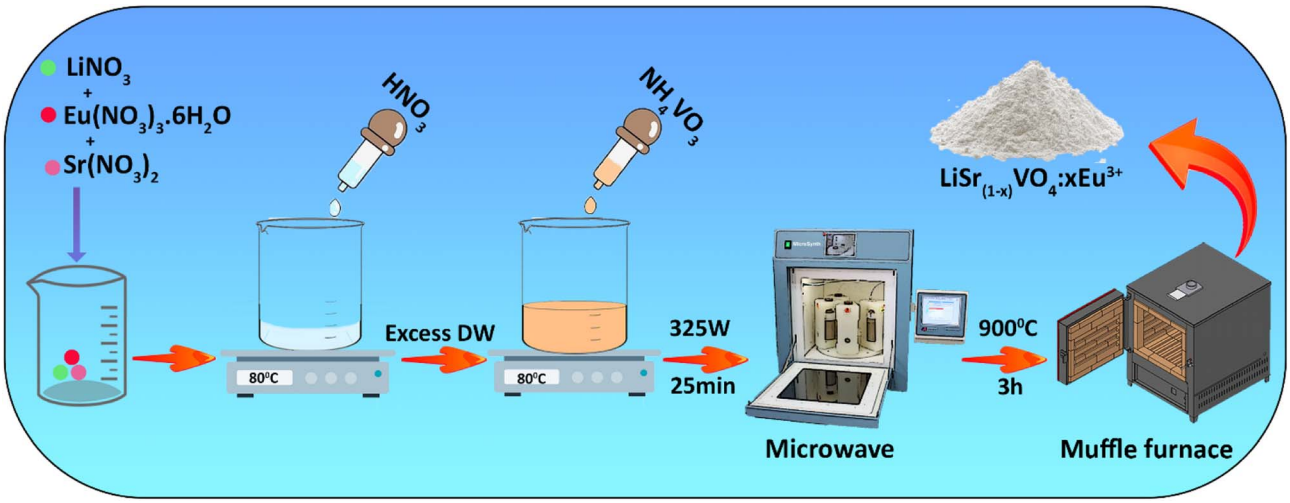

Scheme 1 Schematic illustration of the synthesis of $LiSr_{(1-x)}VO_4:xEu^{3+}$.

LSV:0.015Eu^{3+} solution with a concentration of 2 mg mL^{-1} for 40 s, and then dried at room temperature.

Recommended process for fabrication of the paper-based analytical device (PAD)

The paper-based analytical device (PAD) consists of four main parts: (1) a dark chamber, (2) two UV LED lamps along with optical filters to filter the excitation light and avoid light entering the camera, (3) a USB interface, and (4) a sample slot. A 3D-printed dark chamber consists of defined locations for UV LED lamps (two UV LED lamps ($\lambda = 365$ nm)), two optical filters, and a smartphone camera that can be easily adapted to the fabricated PAD. The device chamber has a hole through the sample slot containing LEBN which enters the PAD device. To reduce optical reflection and eliminate the interference of ambient light, the surface and inside of the dark chamber and the sample slot surface was painted black. The most significant feature of the device (PAD) is its use of parallel excitation light beams, which are emitted by two UV lamps and filtered by two optical filters, ensuring that the light is evenly distributed across all samples inside the device (PAD). By exposing all samples uniformly and simultaneously, systematic errors were reduced, leading to higher quantitative precision. The UV lamps were powered using a USB port connected to a smartphone. Different concentrations of LD and DA were evenly added to the LEBN platform to detect fluorescence quenching.

Determination of quantum yields (QY)

The quantum efficiency of a fluorescence compound is determined by the ratio of photons emitted to photons absorbed. According to the following eqn (1), this work examined the fluorescence intensity and the integrated absorption of LSV:0.015Eu^{3+} with soluble reference rhodamine B.[39]

$$QY_B = QY_R \times \left(\frac{A_R}{A}\right) \times \left(\frac{I}{I_R}\right) \times \left(\frac{n^2}{{n_R}^2}\right) \quad (1)$$

Here, (B) is the quantum efficiency of the LSV:0.015Eu^{3+}, while (R) is the reference quantum efficiency. Additionally, (I) represents the intensity of the fluorescence emission of the sample, (A) represents the sample's absorption, and n is the refractive index of the solvent (in both cases, water has a refractive index of 1.33). To avoid reabsorption effects, it was necessary to dilute the solutions, so their absorbance would be less than 0.1.

Pretreatment of real samples

To evaluate feasibility and reproducibility, LD and DA were detected by the standard addition method in urine, human blood serum, and tap water samples using LSV:0.015Eu^{3+} sensor solutions. To determine the LD and DA concentrations in urine and human serum within the range of linear determination, urine and human blood serum samples were diluted 50 times in deionized water. A human blood serum sample was obtained from a healthy volunteer at Shafa Hospital in Babolsar County. Human blood serum was centrifuged for 3 minutes at 8000 rpm to get the serum. Tap water samples were collected from the University of Mazandaran (Babolsar). Tap water samples were centrifuged to remove impurities and filtered through 0.22 μm membranes. It was diluted 10 times and mixed 1 : 1 with a fluorescent sensor solution to determine LD and DA concentrations.

Results and discussion

The formation of LSV and LSV:0.015Eu^{3+} in the crystalline phase was investigated by X-ray powder diffraction (XRD). According to the XRD patterns of LSV and LSV:0.015Eu^{3+} (Fig. 1A), all the peaks correspond well to the standard values given in JCPDS (No. 053-1242), which indicates a monoclinic structure with a single phase and homogeneous crystalline form. Constant lattice parameters were calculated using the POWD program,[40] where $a = 16.4711$ Å, $b = 11.5122$ Å, and $c = 13.3312$ Å. The constant lattice standard according to the JCPDS card was $a = 16.5374$ Å, $b = 11.6869$ Å, and $c = 13.0087$ Å. Based on the XRD analysis, the high quality and crystallinity of the doped samples were confirmed by the presence of sharp peaks

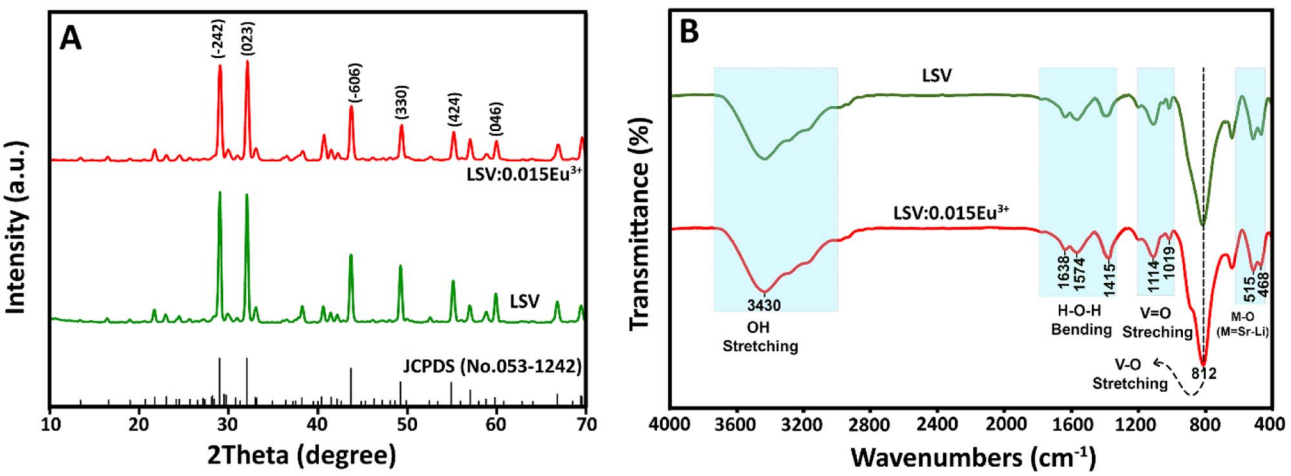

Fig. 1 (A) XRD pattern and (B) FTIR spectra of LSV and LSV:0.015Eu^{3+}.

in the XRD pattern. Furthermore, Eu^{3+} ions enter the lattice by substitution at Sr^{2+} sites, which does not alter the crystal structure of the host. This is due to the similar ionic radii of Eu^{3+} and Sr^{2+} (95 pm and 113 pm, respectively). Therefore, the XRD patterns of both the doped and undoped phosphors remained the same.[41,42] Among the possible occupied ions (Li^+, Sr^{2+}, and V^{5+}), Eu^{3+} ions can only occupy Sr^{2+} sites because a percentage difference (D_r) of less than 30% in ion radii between doped and substituted ions is acceptable.[43] According to eqn (2), the D_r values of the Li^+, Sr^{2+} and V^{5+} cations are 141%, 15.9% and 301%, respectively. Where CN is the coordination number, R_h is the host cation radius, and R_d is the dopant ion radius.

$$D_r = \frac{\left|\left[1 - R_d(CN)_d\right]\right|}{R_h(CN)_h} \times 100 \quad (2)$$

Fourier transform infrared (FTIR) spectra for LSV and LSV:0.015Eu^{3+} are shown in Fig. 1B. The vibration modes in the 400–700 cm^{-1} range are attributed to the M–O (M = Li, Sr) bonds found in the phosphors' monoclinic structure.[44] The peak centered at 812 cm^{-1} corresponds to the absorption band of the $(VO_4)^{3-}$ group, which arises from the V–O stretching vibrational absorption band.[45] Moreover, the two peaks at 1019 cm^{-1} and 1140 cm^{-1} correlate to the V=O bond's stretching vibration.[46,47] The broad band corresponds to the bending vibrations of H–O–H in the range of 1300–1700 cm^{-1}, whereas the broad peak centered about 3430 cm^{-1} belongs to the stretching vibrations of OH, which can be caused by the physical absorption of moisture.[48] The FTIR spectrum for doped samples does not show any significant change in comparison with the host.

The morphology and size of the LSV:0.015Eu^{3+} were evaluated by FESEM and TEM, as shown in Fig. 2A–C. Fig. 2A and B show FESEM images of the synthesized sample, which exhibit nanometer-sized plate-like structures of different sizes. A closer examination of the TEM images (Fig. 2C) revealed the presence of individual nanoplates. Fig. 2D shows the size distribution histogram obtained from the microscopic images. Although a large variation in particle size in the range of 1–40 nm was confirmed, the average particle size was 21 nm.

Energy dispersive X-ray spectroscopy (EDX) and elemental mapping are shown in Fig. S1.† Fig. S1A† shows the FESEM image of the LSV:0.015Eu^{3+} nanoplates, and the corresponding EDX spectrum is shown in Fig. S1B,† confirming the presence of Sr, Eu, V, and O without any impurities. Because EDX analysis is less sensitive to light elements, quantification of the amount of Li was not considered. The uniform distribution of elements in the LSV:0.015Eu^{3+} nanoplates was confirmed by elemental mapping (Fig. S1C–G†).

The elemental composition of the LSV:0.015Eu^{3+} nanoplates was determined using X-ray photoelectron spectroscopy (XPS). The survey scan report for the LSV:0.015Eu^{3+} nanoplates with binding energy (BE) in the range of 0–1400 eV is shown in Fig. 3A. The C 1s peak at 284.3 eV was used as a reference to calibrate the position of other elements in the sample. For vanadium, the binding energy of V $2p_{3/2}$ and V $2p_{1/2}$ can be observed at 518.22 eV and 525.4 eV, respectively (Fig. 3B). Four peaks were observed in the V $2p_{3/2}$ region. The first contribution at 516.47 eV, corresponds to the oxidation state of V^{3+}.[49] The

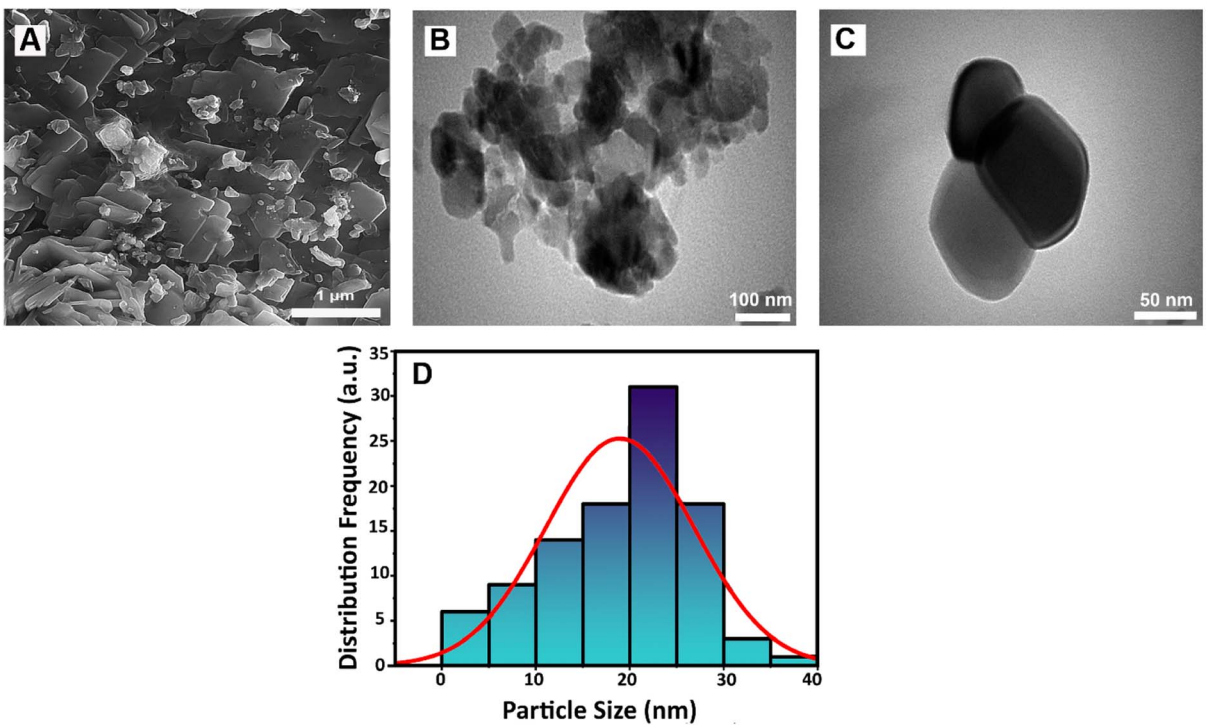

Fig. 2 (A) The FESEM image and (B and C) TEM images, and (D) size distribution histogram of LSV:0.015Eu^{3+} nanoplates.

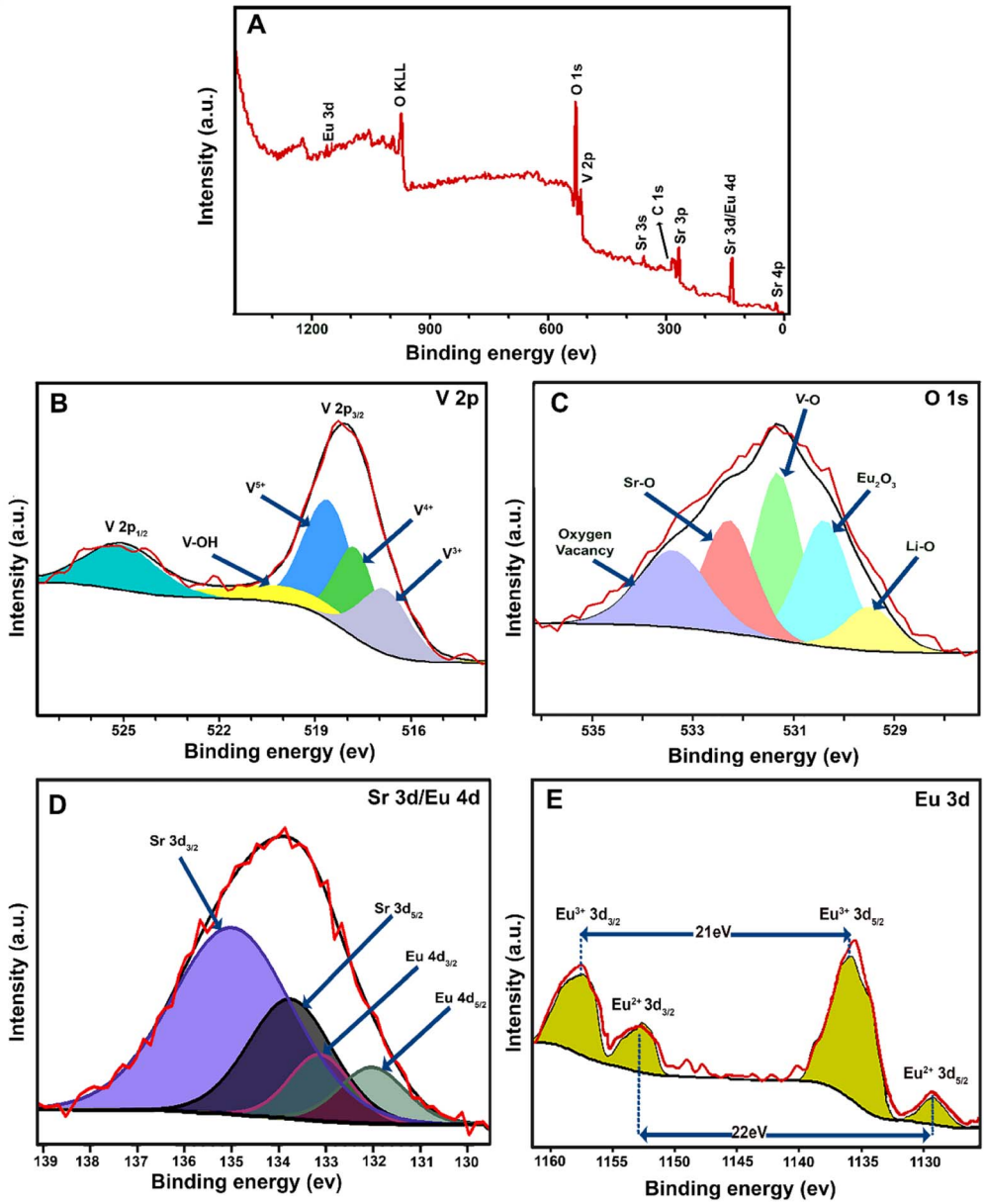

Fig. 3 XPS spectra of LSV:0.015Eu^{3+} nanoplates: (A) survey, (B) V 2p, (C) O 1s, (D) Sr 3d/Eu 4d, and (E) Eu 3d.

second peak at 517.58 eV corresponds to the V^{4+} oxidation state.[50] The third peak, related to the oxidation state of vanadium in LSV:0.015Eu^{3+}, corresponds to the oxidation state of V^{5+}, with a binding energy of 518.27 eV.[51] Finally, the contribution at 519.7 eV can be related to V–OH when moisture is in the sample.[52,53] Fig. 3C shows the XPS spectrum of O 1s, which can be converted into 5 peaks at binding energies of 529.5 eV, 530.4 eV, 531.34 eV, 532.33 eV, and 533.43 eV. Specifically, the binding energy of the O 1s electrons is a measure of the extent to which electrons are localized on the oxygen or in the internuclear region, that is a direct consequence of the nature of the bonding between the oxygen and different cations.[54,55] The peaks at the binding energies of 529.5 eV and 530.4 eV, and 531.34 eV are assigned to the Li–O, Eu_2O_3, and V–O, respectively.[55–57] The V–O peak originated from the lattice oxygen in LSV:0.015Eu^{3+}.[58] Finally, the binding energies of 532.33 eV and 533.44 eV are attributed to Sr–O and oxygen vacancies, respectively.[51,57] Among them, oxygen vacancies are formed to maintain the charge balance during the conversion of vanadium to different oxidation states.[59] Fig. 3D shows the binding energies in the range of 130–140 eV which includes four peaks of Sr 3d and Eu 4d that overlap. A pair of these peaks are related to Sr 3d, which result from spin–orbit splitting between $3d_{5/2}$ (133.76 eV) and $3d_{3/2}$ (134.99 eV). In addition, the other peaks correspond to Eu $4d_{5/2}$ (132.04 eV) and Eu $4d_{3/2}$ (133.10 eV).[60–64] The spin-orbital splitting (Δ) value between $Eu^{3+}(3d_{5/2})$–$Eu^{3+}(3d_{3/2})$ is 20.7 eV and $Eu^{2+}(3d_{3/2})$–$Eu^{2+}(3d_{5/2})$ is 22.3 eV, which were also observed in the XPS spectrum of the sample

(Fig. 3E).[57] The peaks of $Eu^{3+}(3d_{5/2})$ and $Eu^{3+}(3d_{3/2})$ have been determined as 1135.62 eV and 1156.3 eV, respectively. While those of $Eu^{2+}(3d_{5/2})$ and $Eu^{2+}(3d_{3/2})$ have been observed at 1151.52 eV and 1129.1 eV, respectively.[65,66] In addition, the Eu^{3+}/Eu^{2+} ratio was calculated based on the integrated peak area and the result was 7.25, indicating that the oxidation state of Eu^{3+} is preferable.[57]

The stability of the LSV:0.015Eu^{3+} nanoplates under different storage and UV irradiation times was investigated (Fig. S2†). The storage stability of LSV:0.015Eu^{3+} was evaluated after 60 days, and the results showed that it could be stored during this period without losing its intrinsic fluorescence (Fig. S2A†). As shown in Fig. S2B,† the LSV:0.015Eu^{3+} nanoplates exhibited approximately the same fluorescence intensity after 60 min under continuous UV irradiation at 365 nm. In addition, the QY of the as-prepared LSV:0.015Eu^{3+} nanoplates was calculated to be 48%, higher than the reported values of 18.3% for $GdVO_4$:Eu^{3+},[67] 31.2% for $Sr_3La(VO_4)_3$:Eu^{3+},[68] and 39.3% for $LiCa_2SrMgV_3O_{12}$:Eu^{3+}.[69]

This suggests that the prepared LSV:0.015Eu^{3+} could potentially serve as a red-emitting phosphor with a relatively high quantum yield.

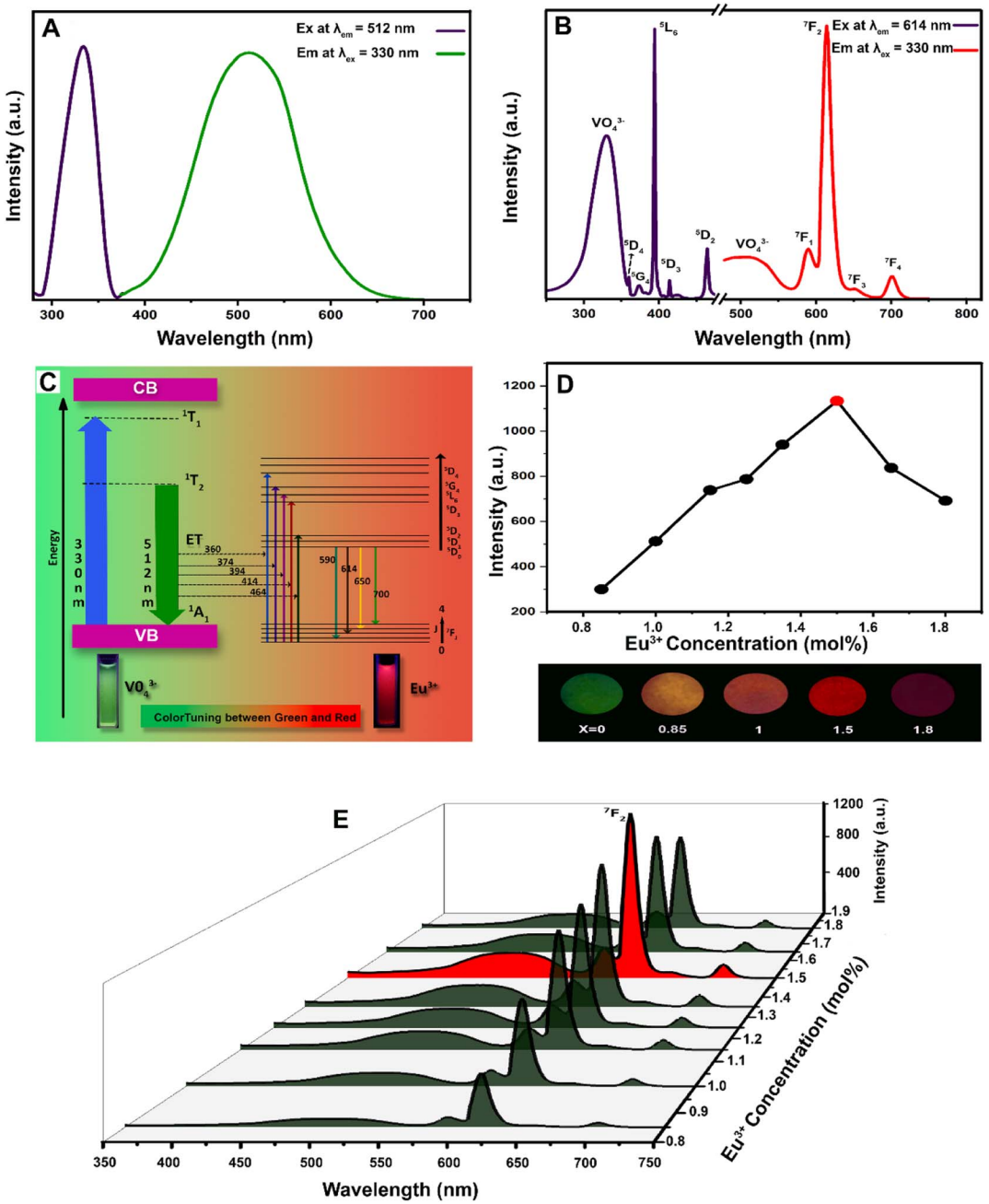

Fig. 4 PLE and PL spectra of (A) LSV host and, (B) LSV:0.015Eu^{3+} nanoplates, (C) energy level diagram of excitation and emission from Eu^{3+} ions incorporated in the LSV host, (D) different luminescent images of LSV:0.015Eu^{3+} nanoplates with optimal Eu^{3+} concentration, and (E) a comparison of LSV:0.015Eu^{3+} nanoplates fluorescence intensity until the optimal Eu^{3+} concentration is reached.

Optical characterization of $LiSr_{(1-x)}V:xEu^{3+}$ nanoplates

The optical characteristics of LSV:0.015Eu^{3+} nanoplates were determined by UV-Vis reflectance and FL spectra. Fig. S3† shows UV-Vis reflectance spectra for LSV and LSV:0.015Eu^{3+} samples between 200–800 nm. Both samples exhibited strong absorption between 270–400 nm centered at 279 nm for LSV and 280 nm for LSV:0.015Eu^{3+}, which is attributed to the charge transfer between O^{2-} (2p orbital) and various V^{5+} levels (3d vacant orbitals) in the $(VO_4)^{3-}$ group.[70] Additionally, the LSV:0.015Eu^{3+} nanoplates have a weak peak at 464 nm attributed to Eu^{3+} ions' f–f transitions.[42,71]

The photoluminescence excitation (PLE) and photoluminescence emission (PL) spectra recorded at room temperature were used to understand the intrinsic photoluminescence properties of the host LSV and LSV:0.015Eu^{3+} nanoplates (Fig. 4). The PLE spectrum with monitoring demonstrates that the LSV sample has an excitation band of 250–380 nm, centered at 330 nm (Fig. 4A).

The host lattice has an absorption band at 330 nm, which is generally related to the excitation from the filled oxygen 2p states of the valence band to the vacant vanadium 3d levels of the conduction band ($O^{2-} \rightarrow V^{5+}$).[72] It can be also attributed to the charge transfer from the $^1A_1$ ground state to the $^1T_1$ and $^1T_2$ excited states of $(VO_4)^{3-}$ groups.[73] Thus, after excitation at 330 nm and charge transfers, the host lattice exhibits an emission spectrum with a broad, intense band at 400–700 nm which is centered at 512 nm (Fig. 4A). In contrast to the LSV excitation spectrum monitored at 512 nm, the LSV:0.015Eu^{3+} nanoplates excitation spectrum consists of sharp spectra that contain Eu^{3+} f–f transitions (Fig. 4B). In addition, the presence of the $(VO_4)^{3-}$ charge transfer band while monitoring the emission of 614 nm, indicates the transfer of energy from $(VO_4)^{3-}$ to Eu^{3+} ions ($O^{2-} \rightarrow Eu^{3+}$). The PLE bands peaks at 360, 374, 394, 414, and 464 nm, correspond to the intra-configurational transitions of Eu^{3+}: $^7F_0 \rightarrow {}^5D_4$, $^7F_0 \rightarrow {}^5G_4$, $^7F_0 \rightarrow {}^5L_6$, $^7F_0 \rightarrow {}^5D_3$, $^7F_0 \rightarrow {}^5D_2$, respectively.[42,48,74] The vanadate group of the LSV:0.015Eu^{3+} nanoplates was less intense than that of the LSV vanadate group based on excitation at 330 nm. Owing to the Eu^{3+} ion addition to the host lattices, the charge transfer of $O^{2-} \rightarrow V^{5+}$ decreased, and the peak intensity of the vanadate group decreased. This reduction depends on the LSV structure and amount of Eu^{3+} ions. Owing to the Eu^{3+} ion addition to the host lattices, the charge transfer of $O^{2-} \rightarrow V^{5+}$ decreases, and the peak intensity of the vanadate group decreases. This reduction depends on the LSV structure and amount of Eu^{3+} ions.[75] In addition to the vanadate spectrum, four characteristic bands of Eu^{3+} ions were observed at 590, 614, 650, and 700 nm in the PL spectrum of the LSV:0.015Eu^{3+} nanoplates. The $^5D_0 \rightarrow {}^7F_1$ (590 nm) transition is related to the magnetic dipole transition and usually has poor intensity.[76] It is well known that the most substantial peak of the electric dipole transition occurs at $^5D_0 \rightarrow {}^7F_2$ (614 nm), which is highly sensitive to the symmetry and acceptor sites occupied by Eu^{3+} ions in the host lattice.[77] When the Eu^{3+} ions occupied the asymmetric center position, the $^5D_0 \rightarrow {}^7F_2$ transition plays a critical role in the luminescent process and has more intensity than the other transitions. In contrast, the $^5D_0 \rightarrow {}^7F_1$ magnetic dipole transition is more intense when the Eu^{3+} is in the position of inversion symmetry.[29] In LSV:0.015Eu^{3+} nanoplates, the Eu^{3+} ions occupied the asymmetric center position, which resulted in the high luminescence intensity of $^5D_0 \rightarrow {}^7F_2$ (614 nm). The emission intensity ratio of $^5D_0 \rightarrow {}^7F_1/{}^5D_0 \rightarrow {}^7F_2$ transitions can measure the site symmetry of rare earth ions, representing the degree of lattice distortion reflected from the inversion symmetry of the LSV lattice surrounding the local crystalline environment of Eu^{3+} ions.[42] Also, the transition $^5D_0 \rightarrow {}^7F_3$ and $^5D_0 \rightarrow {}^7F_4$ correspond to 640 nm and 700 nm, respectively.[29,78] The mechanism for the energy transfer process and color tuning can be seen in Fig. 4C. When LSV:0.015Eu^{3+} nanoplates are excited at 330 nm, electrons are first transported from the $^1A_1$ ground state to the $^1T_1$ level. During this time, excited electrons green lights and eventually return to the ground state after releasing energy form the green lights relax to a lower exciting level ($^1T_2$) and release energy from the.[74] The partially absorbed energy can be transferred to the Eu^{3+} *via* nonradiative resonance or through reabsorption of green light by the Eu^{3+}dopants incorporated into $(VO_4)^{3-}$ groups. LSV can be tuned by adequately introducing Eu^{3+} ions, and different amounts of green and red emissions can be led. This allows for a green-to-red color switch.[70,79]

Generally, three stages can be identified in the excitation and emission of LSV:0.015Eu^{3+} upon exposure to UV radiation. In the first step, the vanadate group absorbed UV radiation. The energy excited by the sublattice of the vanadate group is transferred to the activator ion (Eu^{3+}) in the second step. The last step is de-exciting the Eu^{3+} excited ions, which produces red light.[28] The activator ion concentration affected the luminescence intensity of the LSV:0.015Eu^{3+} nanoplates. Therefore, to determine the optimal Eu^{3+} concentration in the host lattice, the emission intensity of the $^5D_0 \rightarrow {}^7F_2$ transition was evaluated as a function of impurity concentration. When Eu^{3+} ions enter the Sr^{2+} sites in the host lattice, they create an array of vacant oxygen ion sites, which decreases the crystal density.[80,81] It is possible to confirm this claim by examining the XRD pattern recorded from the LSV:0.015Eu^{3+} nanoplates in this study because the peak intensity decreases with the addition of Eu^{3+} ions owing to the loss of crystallinity and decrease in crystal density. In addition to activating the LSV:0.015Eu^{3+} nanoplate lattice and increasing the luminescence intensity, oxygen vacancies act as sensitizers for energy transfer to Eu^{3+} ions.[82] When the concentration of Eu^{3+} ions exceeds the optimum value, excessive oxygen vacancies are created, resulting in the loss of crystallinity and a decrease in luminescence.[83,84] The LSV:0.015Eu^{3+} nanoplate emission peaks are shown in Fig. 4D and E, along with different fluorescence colors, to determine the optimal Eu^{3+} concentration. Fluorescence intensities increased up to 0.015 mol but decreased at higher concentrations.

Investigation of the sensing mechanism for LD and DA detection

In the presence of LD and DA (0.5 mM), the fluorescence intensity of the LSV:0.015Eu^{3+} nanoplates at 614 nm decreases

by more than 50%. First, the quenching principle of fluorescence in the LSV:0.015Eu^{3+} nanoplates was investigated. The fluorescence intensity quenching mechanism is divided into two general categories: dynamic and static quenching. Dynamic quenching can be expressed by the Stern–Volmer eqn (3), and static quenching can be described by the Lineweaver–Burk eqn (4).[85,86]

$$\frac{F}{F_0} = 1 + K_{SV}\, C_q \tag{3}$$

$$\frac{1}{(F_0 - F)} = \frac{1}{F_0} + \frac{K_{LB}}{(F_0 C_q)} \tag{4}$$

The fluorescence intensities in the absence and presence of the analyte are denoted F_0 and F, respectively. K_{SV} is the Stern–Volmer quenching constant, C_q is the analyte concentration, and K_{LB} is the Lineweaver–Burk quenching constant. The magnitude of K_{SV} shows the method's sensitivity to the target molecule.[87] Dynamic quenching involves electron transfer in the excited state, whereas static quenching involves forming a non-fluorescent complex between the analyte and the fluorescent probe in the ground state.[88] In this work, the type of fluorescence quenching mechanism after adding LD and DA was proved in 3 ways. Based on the UV-vis spectrum, the UV absorption curve of LSV:0.015Eu^{3+} nanoplates remained unchanged after adding LD and DA (Fig. 5A). Therefore, dynamic quenching can be confirmed because the absorption spectrum remains the same. On the other hand, in static quenching, the formation of the ground state complex can be determined by changing the absorption spectrum.[89] In addition, the differences between the dynamic and static mechanisms can be attributed to their different dependencies on temperature. The dynamic quenching mechanism was demonstrated through increased quenching rate constants with rising temperature. However, this effect is reversed during static quenching.[90–92] By using the Stern–Volmer equation, it is possible to quantitatively analyze fluorescence quenching at different temperatures (303 K–313 K–323 K) (Fig. 5B and C).[93] As

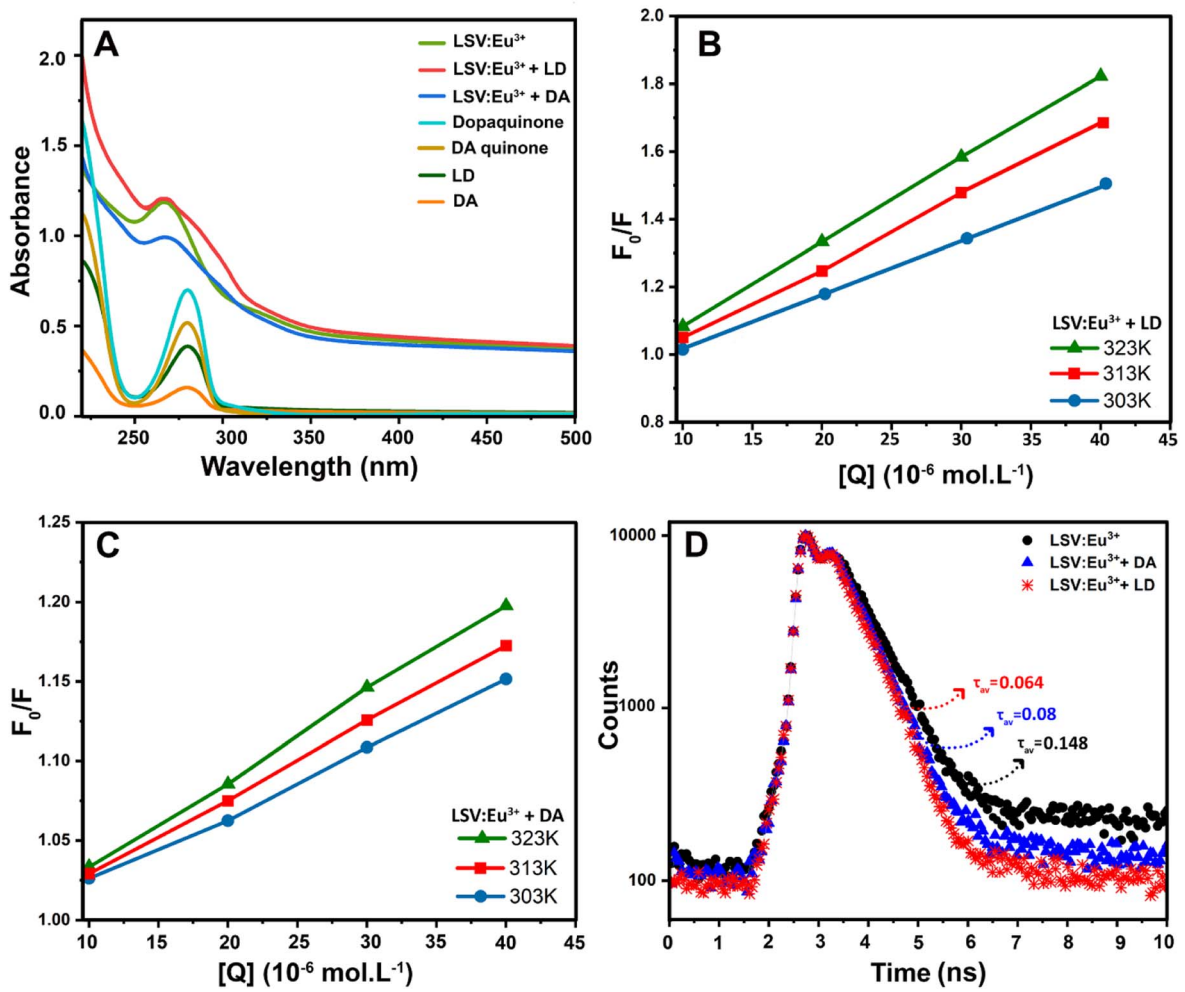

Fig. 5 (A) UV-Vis absorption of LSV:0.015Eu^{3+} nanoplates, LSV:0.015Eu^{3+} + LD, LSV:0.015Eu^{3+} + DA, dopaquinone, DA quinone, LD and DA, (B) Stern–Volmer plots for the LSV:0.015Eu^{3+} + LD solution system at three different temperatures, (C) Stern–Volmer plots for the LSV:0.015Eu^{3+} + DA solution system at three different temperatures, and (D) the FL lifetime decays of LSV:0.015Eu^{3+} nanoplates, LSV:0.015Eu^{3+} + LD, and LSV:0.015Eu^{3+} + DA.

a final investigation of the quenching mechanism, the fluorescence lifetime decay of the LSV:0.015Eu^{3+} nanoplates was investigated in the presence and absence of LD and DA. The fluorescence decay curve and the average fluorescence lifetime of the LSV:0.015Eu^{3+} nanoplates in the presence and absence of LD and DA are shown in Fig. 5D and Table S1,† respectively. The results showed that the lifetime of the samples in the presence of LD and DA was lower than in the absence of LD and DA, which can be attributed to electron transfer which confirms the dynamic quenching mechanism.[88,94] Dynamic quenching generally occurs through electron transfer.[95] Luminescence intensity is determined by electron–hole pair recombination, a well-known mechanism that depends intensely on surface states.[87] LD and DA convert into dopaquinone and dopamine quinone in the basic environment, which can act as electron acceptors from LSV:0.015Eu^{3+} nanoplates.[96,97] The formation of dopaquinone and dopamine quinone can also be confirmed by recording the absorption spectra just before and after a short period of incubation for LD and DA in a basic environment (Fig. 5A).

The quenching phenomenon requires that the energy level of the electron-accepting group is lower than the lowest unoccupied molecular orbital (LUMO) energy of the fluorescent material, or that non-covalent interactions occur between the fluorescent material and analyte molecules.[98–100] As shown in Fig. 6, upon excitation of the LSV:0.015Eu^{3+} nanoplates, electrons were promoted into the conduction band from their valence band, resulting in the formation of a positively charged hole in the valence band and a free electron in the conduction band. Accordingly, the recombination of electrons and holes results in fluorescence emission. The electrons were transferred from the 2p orbital of oxygen to the 4f orbital of Eu^{3+}. The highest-intensity fluorescence signal at 614 nm originates from the $^5D_0 \rightarrow {}^7F_2$ transition of Eu^{3+}, whereas the other $^5D_0 \rightarrow {}^7F_j$ transitions of Eu^{3+} are too weak. The electron–hole recombination of the LSV:0.015Eu^{3+} nanoplates is disturbed when LD or DA (which acts as an electron acceptor) is added to the sensor solution. Specifically, charge transfer occurs between the excited state and LUMO of the LD or DA molecule rather than the $^5D_0$ state of Eu^{3+}, which reduces the number of electrons in the $^5D_0$ state. Therefore, the decrease in charge transfer to the $^5D_0$ state decreased the emission from the Eu centers. In addition, an increase in LD or DA concentrations accelerated the quenching rate of the fluorescence intensity.[101]

Optimization of detection parameters

To reach the optimal conditions for LD and DA detection, several influential variables such as pH, LSV:0.015Eu^{3+} solution concentration, and hold time were evaluated using the one-factor-at-a-time (OFAT) method followed by the statistical approach of Response Surface Methodology (RSM)–CCD matrix *via* Design-Expert 12 software. The optimization process for a variety of parameters can be simplified by first utilizing a classical method such as the OFAT method to identify the optimal range for each factor before using the more advanced RSM methodology. LSV:0.015Eu^{3+} nanoplates interact relatively weakly with LD and DA at an acidic pH. As pH increases, fluorescence quenching efficiency $(F_0/F) - 1$ (where F_0 and F represent the fluorescence intensity before and after the addition of LD and DA, respectively) increases gradually until it reaches 9 as the maximum (Fig. S4A and B†).

CCD, categorized as a set of advanced 'design of experiments' (DoE) methods, was used for a more accurate optimization. This method provides a statistical analysis of the factors

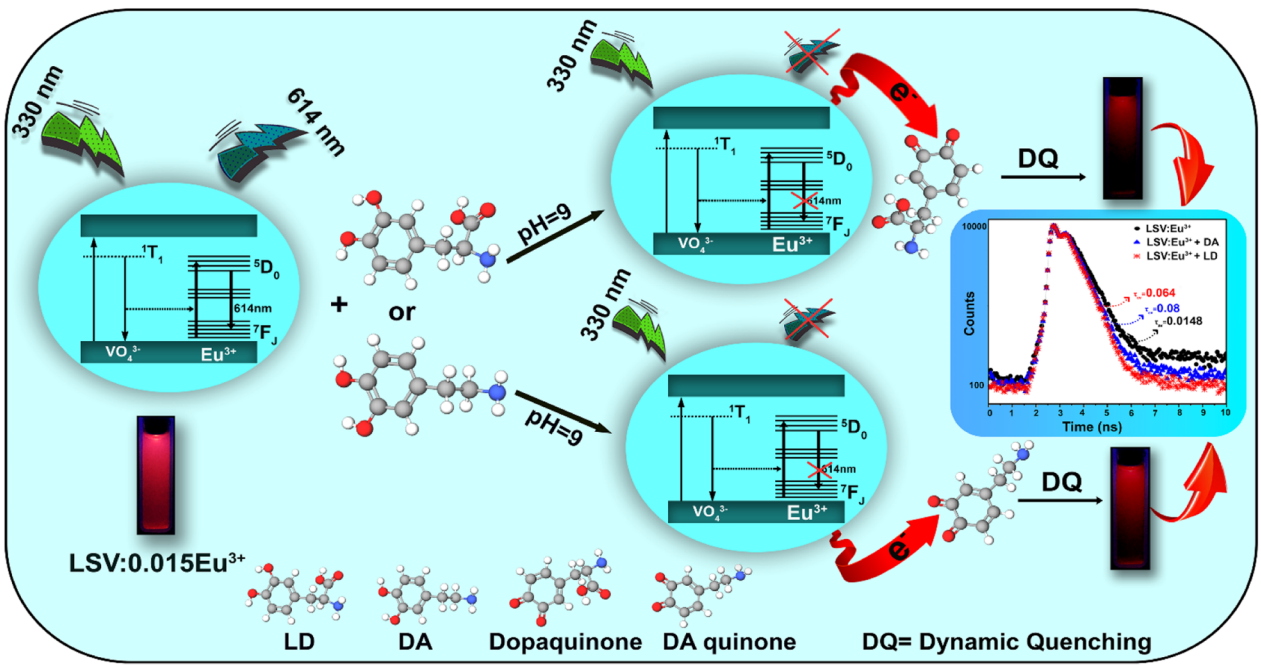

Fig. 6 Schematic illustration of the working principle for LD and DA detection based on quenching FL of LSV:0.015Eu^{3+} nanoplates.

that affect the response of the sensor. According to Fig. S5 and S6,† the results of effective parameters such as pH, LSV:0.015Eu^{3+} solution concentration, and hold time for LD and DA detection show that the model designed is accurate and reliable. In addition, the results of the model designed with the CCD matrix to optimize the effective parameters in the determination of LD and DA were consistent with the optimization results obtained using the OFAT method. The optimal parameters investigated in this work were 5 min for LD and 7 min for DA, pH 9, and 350 ppm concentration for LD and DA.

The sensitivity and selectivity of the LSV:0.015Eu^{3+} nanoplates

To investigate the detection sensitivity of the LSV:0.015Eu^{3+} nanoplates fluorescent sensor under optimal conditions, the sensor's ability to detect LD and DA was determined by adding different concentrations of analyte at an excitation wavelength of 330 nm. The fluorescence intensities of the LSV:0.015Eu^{3+} nanoplates after adding LD and DA were measured quantitatively, as shown in Fig. 7A and B. Based on these results, the analyte concentration affects the fluorescence quenching of the sensor. Thus, the fluorescence intensity of the LSV:0.015Eu^{3+} nanoplates decreased gradually with increasing LD and DA concentrations without altering the spectral emission wavelength. When the LD concentration was between 1–40 μM, a linear relationship with the Stern–Volmer equation $F_0/F = 0.0091C_{LD} + 0.0076$, and a correlation coefficient of 0.9972 was used to evaluate the effect of quenching of the LSV:0.015Eu^{3+} nanoplates solution by LD, where F_0 and F are the fluorescence intensity of the solution without analyte and the intensity of the solution is in the presence of the analyte, respectively (Fig. 7C). Similarly, in the concentration range of 2–50 μM, there is a linear relationship with the Stern–Volmer equation $F_0/F = 0.0065C_{DA} + 0.0093$ with a correlation coefficient of 0.9976 between DA concentration and fluorescence response (Fig. 7D). In addition, under UV lamp irradiation at 365 nm, it was observed by the naked eye that the red fluorescence of the LSV:0.015Eu^{3+} nanoplates gradually decreased as concentrations of LD and DA increased (Fig. 7E(a and b)). Based on the

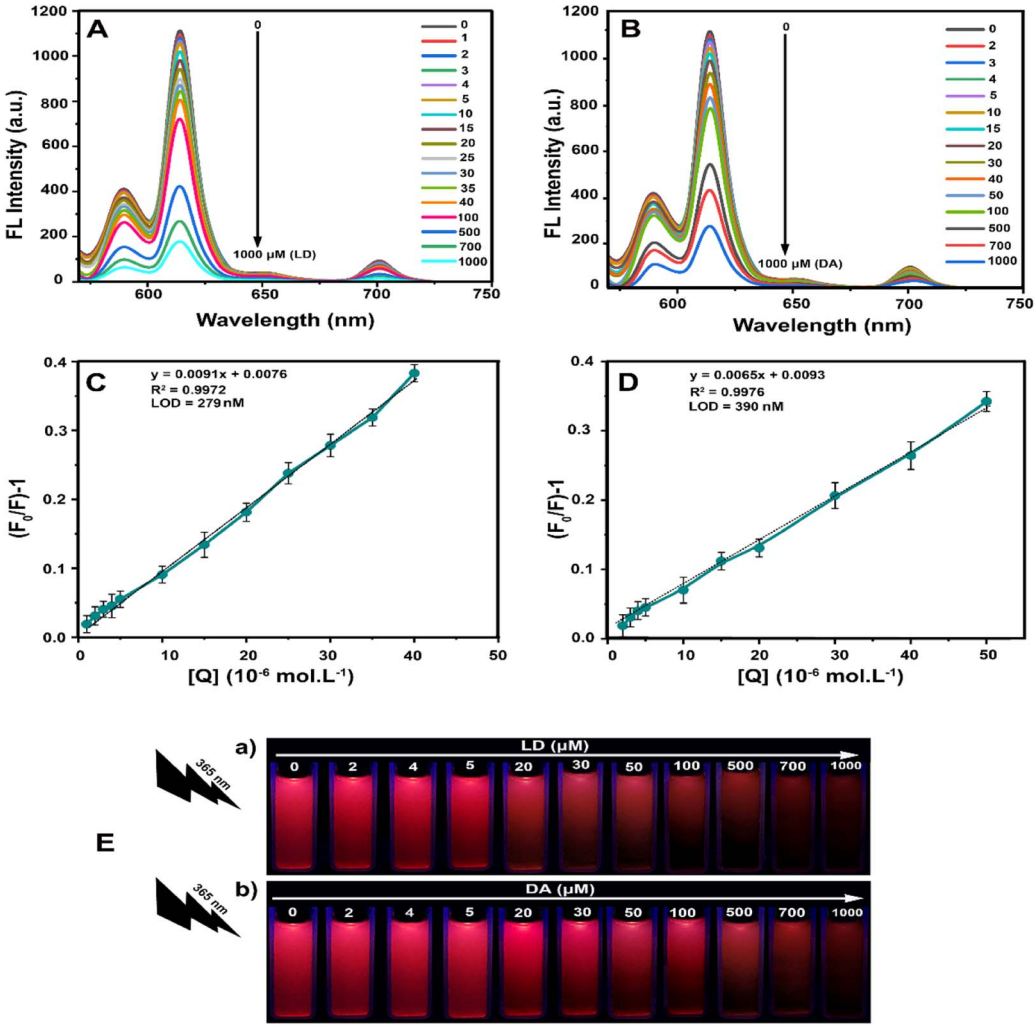

Fig. 7 Sensitive detection of LD and DA with the LSV:0.015Eu^{3+} fluorescent sensor. Fluorescence spectra of different concentrations of (A) LD, (B) DA; the corresponding plots of fluorescence intensity against concentration for (C) LD, (D) DA; (E) photographs of the LSV:0.015Eu^{3+} nanoplates after the interaction with increasing concentrations of (a) LD, (b) DA under 365 nm UV light.

quantitative analysis, the limit of detection (LOD) of the fabricated fluorescent sensors was calculated using equation $3\sigma/K_{SV}$ (K_{SV} represents the slope of the calibration line and σ is the standard deviation of the measured blank solution signal), which was reported as 279 nM and 390 nM, respectively, for LD and DA.[92,102]

In addition, different detection methods with different DA and LD detection limits are reported in Table S2.† Selectivity is one of the most critical properties of fluorescent sensors. Consequently, the LSV:0.015Eu^{3+} nanoplates were examined for the selectivity of LD and DA based on its fluorescence signal response with various interfering agents (glutamine, sodium chloride, L-cysteine, calcium chloride, ascorbic acid (AA), glucose, urea, and aspirin). Under optimal conditions, interfering agents, LD and DA were used at 700 μM concentrations. According to Fig. 8A and B, the fluorescence intensity and color of the solution have barely changed after adding other interferents compared to the control group. After adding LD and DA, there is a significant reduction in fluorescence intensity, while the color of the solution has changed significantly. These results eliminate the influences of the examined interfering substances, and the detection of LD and DA can be confirmed by the high selectivity of LSV:0.015Eu^{3+} nanoplates.

Smartphone sensing platform for detection of LD and DA

As a complement to fluorescence spectrophotometer tests of LSV:0.015Eu^{3+} nanoplates, paper-based methods have been used because of their simplicity, robustness, and ability to monitor real-time results. A bacterial cellulose nanopaper was chosen as a substrate for its capillary effect, biodegradability, biocompatibility, hydrophilicity, and ability to wick aqueous solutions. For this purpose, LEBN (LSV:0.015Eu^{3+} bacterial cellulose nanopaper) was prepared by immersing the appropriate cellulose nanopaper in the LSV:0.015Eu^{3+} solution. The scanning electron microscopy images in Fig. S7A and B† demonstrate that LSV:0.015Eu^{3+} nanoplates were successfully coated on bacterial cellulose nanopaper. Though the fluorescence visual detection could be achieved by the LEBN without extra equipment, it is not highly effective since the naked eye cannot detect trivial changes in fluorescence intensity. As a result, it is imperative to develop a method for real-time/*in situ* detection that is visual, quantitative, and instrument-free. Therefore, it is possible to visually and quantitatively detect LD and DA at a low cost. To demonstrate that the platform is capable of capturing data from sensing and removing external light fluctuations, a PAD was designed. It is a fast, efficient technology that does not require expensive equipment and is extremely cost-effective.[103] An overview of the design of the PAD and the placement of the smartphone on the PAD can be found in Fig. 9A and B. A smartphone is attached to the PAD. Different concentrations of LD and DA were uniformly added to the treated LEBN to determine the change in fluorescence intensity. The fluorescence quenching changes observed on bacterial cellulose nanopaper under UV light after adding different amounts of LD and DA are shown in Fig. 9C and D, respectively. The images were taken using a smartphone (Huawei NOVA 7i) which shows that the increase in the analyte concentration, decreases the fluorescence intensity of LEBN. Although the color changes can be observed visually, to avoid deviations caused by visual acuity and to improve the accuracy of this method, the RGB values were analyzed by a color recognizer application (Grab) using only the red color of the case (Fig. 9E). The data obtained from the smartphone application (Grab) were analyzed based on different LD and DA values by displaying them on the calibration curve. According to the Stern–Volmer equation, the calibration curves of LD and DA showed relatively good linearity, as shown in Fig. 9F and G, with a linear calibration curve in the range of 1–30 μM with a correlation

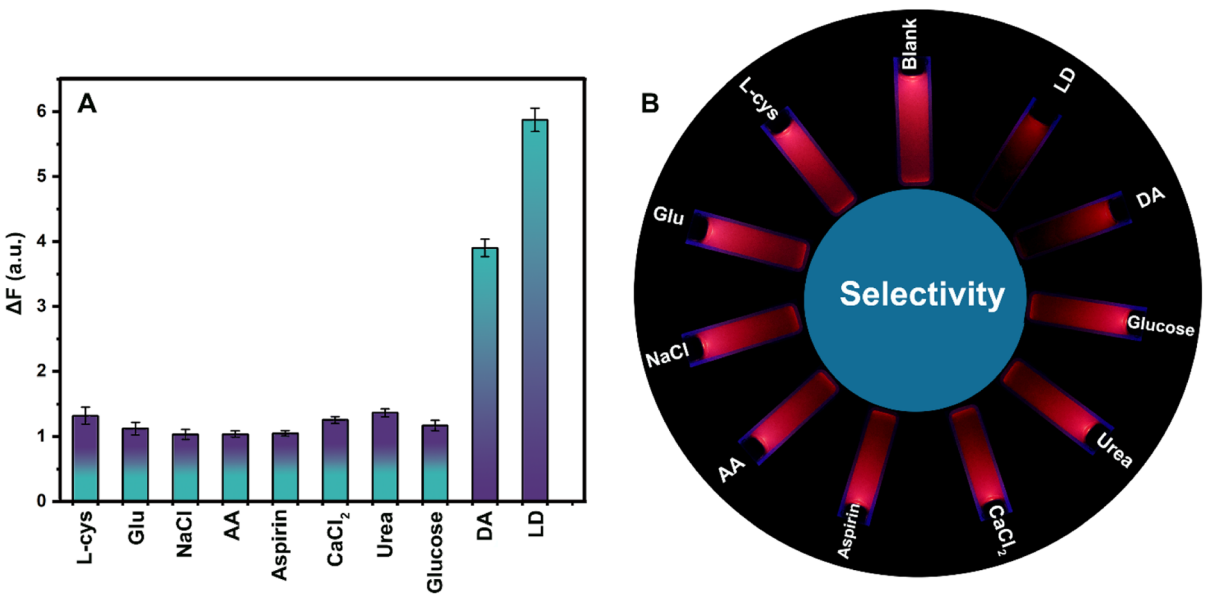

Fig. 8 (A) Selectivity of the LSV:0.015Eu^{3+} fluorescent sensor towards LD and DA, (B) fluorescent photos of the LSV:0.015Eu^{3+} fluorescent sensor upon addition of different interfering agents under a UV lamp.

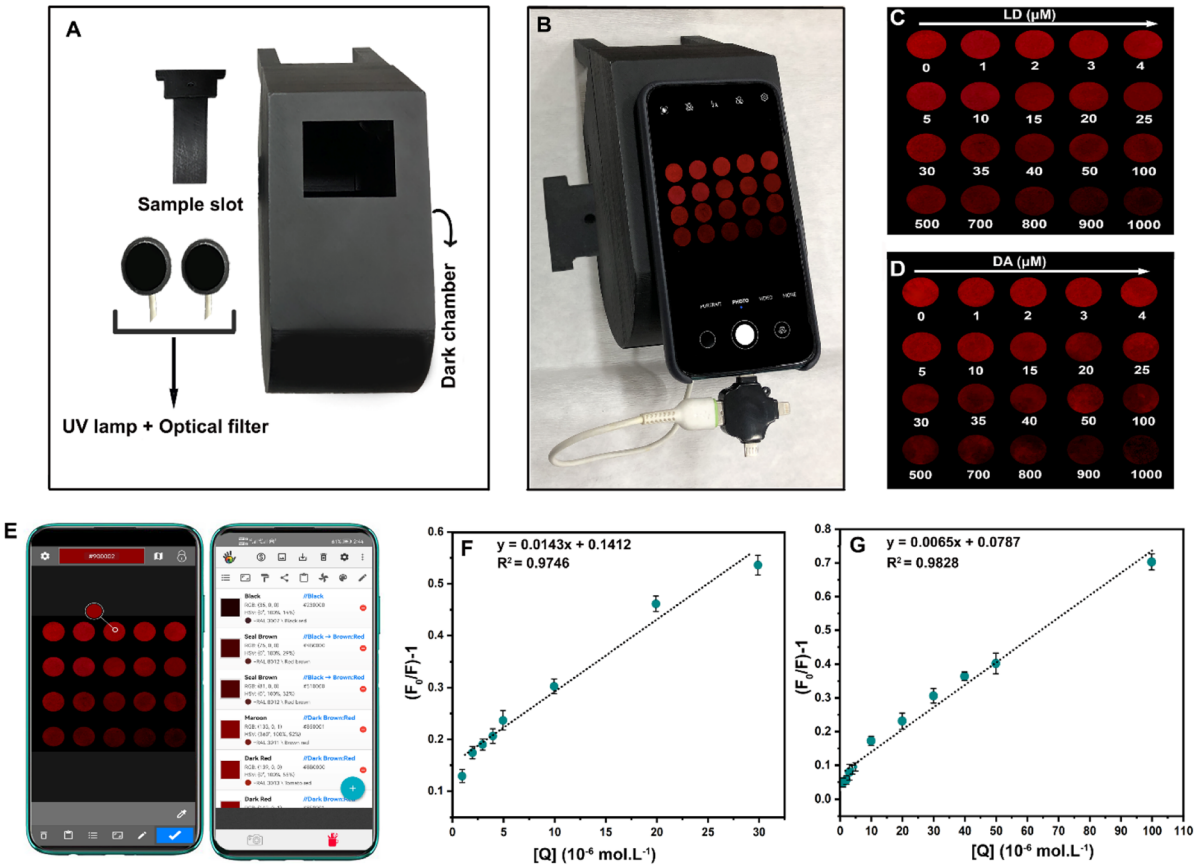

Fig. 9 (A) The structure of the 3D-printed PAD sensing platform, (B) photo of the constructed smartphone sensing platform, (C) LD and (D) DA concentration added to LEBN, (E) RGB analysis of the generated images *via* a color Grab, (F) LD and (G) DA calibration curves plotting intensity change of LEBN dye fluorescence quenching intensity based on the Stern–Volmer equation.

coefficient of 0.9746 for LD, and in the range of 1–100 μM with a correlation coefficient of 0.9828 for DA.

Detection of LD and DA in real samples

In real diagnostic applications, the presence of catecholamines, such as DA and LD, in urine can be used to accurately gauge the activity of the sympathoadrenal system. Determination of the DA concentration in urine is essential for diagnosing pheochromocytoma tumors and conditions such as PD.[104] Under optimal conditions, in urine, human serum, and tap water samples, DA and LD concentrations were measured based on the calibration curves. As shown in Table S3,† the detection results are obtained. DA and LD standards with different concentrations were used for the real samples. The standard deviations ($n = 3$) were all less than 6%, and the average recoveries ranged from 96 to 107%.

Conclusions

In summary, LSV:0.015Eu^{3+} nanoplates were synthesized using a microwave-assisted co-precipitation method with suitable quantum efficiency (48%) and high selectivity towards LD and DA. In addition, the LSV:0.015Eu^{3+} nanoplates exhibited excellent stability in terms of storage time and UV radiation. Various optical and structural identification methods, such as XRD, FTIR, FESEM, TEM, EDX, XPS, DRS, UV-Vis, fluorescence spectroscopy, and fluorescence lifetime decay spectroscopy, were used to examine the synthesized samples. The results obtained from the analyses confirmed the capability of the LSV:0.015Eu^{3+} nanoplates in optical sensors. The sensor was prepared under the optimal conditions determined by OFAT followed by the statistical approach of the RSM–CCD matrix using Design-Expert 12 software, which is capable of measuring the concentrations of LD and DA *via* a dynamic mechanism. In addition, a sensing platform based on 3D printing technology was designed for rapid and sensitive detection using LEBN. Hence, the smartphone provides a reliable approach for rapid and accurate visual quantification, which can quantify the fluorescence intensity change by measuring RGB using a color recognition application (Grab). The LSV:0.015Eu^{3+} fluorescent sensor is fast, sensitive, and selective for detecting LD and DA concentrations, making it an excellent tool for ameliorating the side effects of PD. In addition, the LSV:0.015Eu^{3+} fluorescence sensor showed acceptable reproducibility and was used for the analysis of real human urine, blood serum, and tap water samples with a recovery of 96–107%.

Ethical approval

Human blood serum samples were collected according to the relevant local laws of Iran and guidelines of the hospital in Babolsar, Mazandaran, Iran. As the study samples were anonymous, written consent was not required by the ethics committee and the study was approved by the institutional study of the Department of Applied Chemistry, University of Mazandaran, Babolsar, Iran.

Author contributions

The manuscript was written through the contributions of all authors. All authors have approved the final version of the manuscript.

Conflicts of interest

There are no conflicts of interest to declare.

Notes and references

1 Z. Han, R. Tian, P. Ren, W. Zhou, P. Wang, M. Luo, S. Jin and Q. Jiang, *BMC Med. Genet.*, 2018, **19**, 215.
2 V. Di Battista and E. Hey-Hawkins, *J. Pharm. Sci.*, 2022, **111**, 1262–1279.
3 Y. Wang, H. Zhang and M. Chen, *Anal. Chim. Acta*, 2021, **1157**, 338379.
4 D. Meder, D. M. Herz, J. B. Rowe, S. Lehéricy and H. R. Siebner, *Neuroimage*, 2019, **190**, 79–93.
5 D. Aarsland, L. Batzu, G. M. Halliday, G. J. Geurtsen, C. Ballard, K. Ray Chaudhuri and D. Weintraub, *Nat. Rev. Dis. Primers*, 2021, **7**, 47.
6 F. Haddad, M. Sawalha, Y. Khawaja, A. Najjar and R. Karaman, *Molecules*, 2018, **23**, 40.
7 C. Chen, C. Zou, L. Li, H. Yu, J. Zhu, J. Liu and W. Huang, *Talanta*, 2020, **214**, 120817.
8 S. W. Park, T. E. Kim and Y. K. Jung, *Anal. Chim. Acta*, 2021, **1165**, 338513.
9 D. Ji, N. Xu, Z. Liu, Z. Shi, S. S. Low, J. Liu, C. Cheng, J. Zhu, T. Zhang and H. Xu, *Biosens. Bioelectron.*, 2019, **129**, 216–223.
10 J. Bicker, A. Fortuna, G. Alves and A. Falcão, *Anal. Chim. Acta*, 2013, **768**, 12–34.
11 J. Wu, Z. Li and L. Jia, *Microchim. Acta*, 2019, **186**, 1–9.
12 R. Li, D. Zhang, X. Li and H. Qi, *Bioelectrochemistry*, 2022, **146**, 108148.
13 Q. Liu, X. Chen, Z.-W. Kang, C. Zheng and D.-P. Yang, *Nanoscale Res. Lett.*, 2020, **15**, 24.
14 S. Abbasi-Moayed, A. Bigdeli and M. R. Hormozi-Nezhad, *ACS Appl. Mater. Interfaces*, 2020, **12**, 52976–52982.
15 Y. Luo, L. Zhang, L. Zhang, B. Yu, Y. Wang and W. Zhang, *ACS Appl. Mater. Interfaces*, 2019, **11**, 15998–16005.
16 Y.-Z. Ding, W.-F. Wang, T. Chai, Y. Qiang, Y.-P. Shi and J.-L. Yang, *Talanta*, 2019, **197**, 113–121.
17 S. Y. Lee, M. Lin, A. Lee and Y. I. Park, *Nanomaterials*, 2017, **7**, 411.
18 N. L. Rosi and C. A. Mirkin, *Chem. Rev.*, 2005, **105**, 1547–1562.
19 S. Babu, V. Reddy Prasad, D. Rajesh and Y. C. Ratnakaram, *J. Mol. Struct.*, 2015, **1080**, 153–161.
20 S. Nsanzamahoro, W.-F. Wang, Y. Zhang, Y.-P. Shi and J.-L. Yang, *Talanta*, 2021, **231**, 122369.
21 D. Chávez-García, P. Sengar, K. Juárez-Moreno, D. L. Flores, I. Calderón, J. Barrera and G. A. Hirata, *J. Mater. Res. Technol.*, 2021, **10**, 797–807.
22 H. Zeng, X. Li, M. Sun, S. Wu and H. Chen, *Molecules*, 2017, **22**, 753.
23 A. Escudero, C. Carrillo-Carrión, M. V. Zyuzin, S. Ashraf, R. Hartmann, N. O. Núñez, M. Ocaña and W. J. Parak, *Nanoscale*, 2016, **8**, 12221–12236.
24 H. Zhang, T. Chen, S. Qin, J. Huang and X. Wu, *Dalton Trans.*, 2022, **51**, 5577–5586.
25 Y. Matsushima, T. Koide, M. Hiro-Oka, M. Shida, A. Sato, S. Sugiyama and M. Ito, *J. Am. Ceram. Soc.*, 2015, **98**, 1236–1244.
26 M. A. Gómez Torres, G. H. Gauthier, A. M. Kaczmarek, M. Huvé, P. Roussel, V. Dupray, L. Yuan, A. Zadoya and M. Colmont, *Am. Chem. Soc.*, 2020, **59**, 5929–5938.
27 H. Gu, J. Wang, Z. Wang, J. Yao, J. Zhang and Z. Du, *Opt. Mater.*, 2019, **96**, 109254.
28 S. Tang, M. Huang, J. Wang, F. Yu, G. Shang and J. Wu, *J. Alloys Compd.*, 2012, **513**, 474–480.
29 H.-H. Zeng, H. Wu, D. Peng, F. Liu, W.-G. Shi and J.-D. Qiu, *ACS Sens.*, 2018, **3**, 1569–1575.
30 L. Prodi, E. Rampazzo, F. Rastrelli, A. Speghini and N. Zaccheroni, *Chem. Soc. Rev.*, 2015, **44**, 4922–4952.
31 L. Zhang, S. Lyu, Z. Chen and S. Wang, *J. Nanomater.*, 2018, **8**, 352.
32 Z. Zhang, N. Ma, S. Yao, W. Han, X. Li, H. Chang and Y.-Y. Wang, *ACS Sustain. Chem. Eng.*, 2021, **9**, 5827–5837.
33 F. G. Torres, O. P. Troncoso, K. N. Gonzales, R. M. Sari and S. Gea, *Med. Devices Sens.*, 2020, **3**, e10102.
34 L. Yu, L. Feng, L. Xiong, S. Li, Q. Xu, X. Pan and Y. Xiao, *Nanoscale*, 2021, **13**, 11188–11196.
35 H. J. Kitchen, S. R. Vallance, J. L. Kennedy, N. Tapia-Ruiz, L. Carassiti, A. Harrison, A. G. Whittaker, T. D. Drysdale, S. W. Kingman and D. H. Gregory, *Chem. Rev.*, 2014, **114**, 1170–1206.
36 J. Miranda de Carvalho, D. Van der Heggen, L. I. D. J. Martin and P. F. Smet, *Dalton Trans.*, 2020, **49**, 4518–4527.
37 L. Wang, M. Xu, R. Sheng, L. Liu and D. Jia, *J. Alloys Compd.*, 2013, **579**, 343–347.
38 Y. Liu, H. Xiong, N. Zhang, Z. Leng, R. Li and S. Gan, *J. Alloys Compd.*, 2015, **653**, 126–134.
39 K.-L. Wong, J.-C. G. Bünzli and P. A. Tanner, *J. Lumin.*, 2020, **224**, 117256.
40 E. Wu, *J. Appl. Crystallogr.*, 1989, **22**, 506–510.
41 H. Zhou, N. Guo, Q. Liang, Y. Ding, Y. Pan, Y. Song, R. Ouyang, Y. Miao and B. Shao, *Ceram. Int.*, 2019, **45**, 16651–16657.
42 X. Zhou, L. Chen, S. Jiang, G. Xiang, L. Li, X. Tang, X. Luo and Y. Pang, *Dyes Pigm.*, 2018, **151**, 219–226.

43 P. Kumar, S. Singh, I. Gupta, K. Nehra, V. Kumar and D. Singh, *J. Lumin.*, 2022, **252**, 119338.
44 X. Guo, S. Song, X. Wang, X. Jiang, W. Lv, X. Yu, Y. Han and L. Wang, *Opt. Mater.*, 2019, **96**, 109342.
45 P. Biswas, V. Kumar, V. Sharma, A. Bedyal, N. Padha and H. Swart, *Phys. B*, 2018, **535**, 221–226.
46 L. W. Shan, W. Li, Z. Li, J. B. Mi, D. Sun, P. Li and L. M. Dong, *Appl. Mech. Mater.*, 2013, **320**, 654–660.
47 H. Mahandra, R. Singh and B. Gupta, *Hydrometallurgy*, 2020, **196**, 105405.
48 Z. Ghubish, R. Kamal, H. R. Mahmoud, M. Saif, H. Hafez and M. El-Kemary, *RSC Adv.*, 2021, **11**, 18552–18564.
49 J. Zeng, Y. Yang, C. Li, J. Li, J. Huang, J. Wang and J. Zhao, *Electrochim. Acta*, 2017, **247**, 265–270.
50 L.-W. Dong, R.-G. Xu, P.-P. Wang, S.-C. Sun, Y. Li, L. Zhen and C.-Y. Xu, *J. Power Sources*, 2020, **479**, 228793.
51 Y. Bourlier, M. Frégnaux, B. Bérini, A. Fouchet, Y. Dumont and D. Aureau, *Appl. Surf. Sci.*, 2021, **553**, 149536.
52 T. Kokulnathan and S.-M. Chen, *ACS Sustain. Chem. Eng.*, 2019, **7**, 4136–4146.
53 M. Michalska, J. B. Jasiński, J. Pavlovsky, P. Żurek-Siworska, A. Sikora, P. Gołębiewski, A. Szysiak, V. Matejka and J. Seidlerova, *J. Lumin.*, 2021, **233**, 117934.
54 G. D. Khattak and N. Tabet, *J. Electron Spectrosc. Relat. Phenom.*, 2004, **136**, 257–264.
55 D. Govindarajan, F. J. Johanson, V. Uma shankar, M. J. Salethraj and R. Gopalakrishnan, *J. Mater. Sci.: Mater. Electron.*, 2021, **32**, 19434–19445.
56 J. Prakash, U. Prasad, X. Shi, X. Peng, B. Azeredo and A. M. Kannan, *J. Power Sources*, 2020, **448**, 227418.
57 I. Charak, M. Manhas, A. K. Bedyal, S. Singh, A. Srivastava, H. C. Swart and V. Kumar, *J. Alloys Compd.*, 2021, **869**, 159363.
58 M. Chen, K. Qiu, P. Zhang, W. Zhang and Q. Yin, *Ceram. Int.*, 2019, **45**, 22547–22552.
59 Y. Qu and G. Wang, *J. Mater. Chem.*, 2022, **10**, 5990–5997.
60 U. Manju, V. P. S. Awana, H. Kishan and D. D. Sarma, *Phys. Rev. B: Condens. Matter Mater. Phys.*, 2006, **74**, 245106.
61 J. H. Oh, H. M. Noh, J. H. Jeong, S. H. Park, B. C. Choi and J. S. Bae, *Opt. Mater.*, 2021, **116**, 111092.
62 M. Y. A. Yagoub, H. C. Swart, L. L. Noto, J. H. O'Connel, M. E. Lee and E. Coetsee, *J. Lumin.*, 2014, **156**, 150–156.
63 M. Y. A. Yagoub, H. C. Swart and E. Coetsee, *Vac*, 2021, **191**, 110362.
64 U. Kumar, S. Upadhyay and P. A. Alvi, *Phys. B*, 2021, **604**, 412708.
65 Y. Hua and J. S. Yu, *Ceram. Int.*, 2021, **47**, 18003–18011.
66 F. Li, Z. Li, X. Wang, M. Zhang, Y. Shen, P. Cai and X. He, *J. Alloys Compd.*, 2017, **692**, 10–21.
67 V. Muhr, M. Buchner, T. Hirsch, D. J. Jovanović, S. D. Dolić, M. D. Dramićanin and O. S. Wolfbeis, *Sens. Actuators, B*, 2017, **241**, 349–356.
68 J. Zhou, F. Huang, J. Xu, H. Chen and Y. Wang, *J. Mater. Chem. C*, 2015, **3**, 3023–3028.
69 H. Chen, J. Zhou, H. Zhang and Z. Hu, *Opt. Mater.*, 2019, **89**, 132–137.
70 X. Zhang, Z. Zhu, Z. Guo, Z. Sun, L. Zhou and Z.-c. Wu, *Ceram. Int.*, 2018, **44**, 16514–16521.
71 X. Zhou, J. Zhang, L. Chen, Y. Li, G. Xiang, S. Jiang, L. Li, X. Tang, Z. Cao and G. Xie, *J. Am. Ceram. Soc.*, 2021, **104**, 2721–2729.
72 N. Sawala and S. Omanwar, *J. Alloys Compd.*, 2016, **686**, 287–291.
73 X. Huang and H. Guo, *Ceram. Int.*, 2018, **44**, 10340–10344.
74 F. Kang, L. Li, J. Han, D. Y. Lei and M. Peng, *J. Mater. Chem. C*, 2017, **5**, 390–398.
75 M. R. Dolgos, A. M. Paraskos, M. W. Stoltzfus, S. C. Yarnell and P. M. Woodward, *J. Solid State Chem.*, 2009, **182**, 1964–1971.
76 Y. Wang, W. Qin, J. Zhang, C. Cao, S. Lü and X. Ren, *Opt. Commun.*, 2009, **282**, 1148–1153.
77 T. Jeyakumaran, N. V. Bharathi, P. Sriramachandran, R. Shanmugavel and S. Ramaswamy, *J. Inorg. Organomet. Polym. Mater.*, 2021, **31**, 674–682.
78 Q. Tang, Y. Wu, K. Qiu, W. Zhang and J. Wang, *Ceram. Int.*, 2018, **44**, 6192–6200.
79 M. Rajendran, S. K. Samal and S. Vaidyanathan, *J. Alloys Compd.*, 2020, **815**, 152631.
80 F. S. Hegner, D. Forrer, J. R. Galán-Mascarós, N. López and A. Selloni, *J. Phys. Chem. Lett.*, 2019, **10**, 6672–6678.
81 M. V. Ganduglia-Pirovano, A. Hofmann and J. Sauer, *Surf. Sci. Rep.*, 2007, **62**, 219–270.
82 P. Biswas and V. Kumar, *Mater.*, 2020, **28**, 1018–1023.
83 P. Biswas, V. Kumar, N. Padha and H. Swart, *J. Mater. Sci.: Mater. Electron.*, 2017, **28**, 6159–6168.
84 P. Du and J. S. Yu, *Dyes Pigm.*, 2017, **147**, 16–23.
85 T. Zhu, Q. Gou, Y. Yang, Y. Zhang and M. Chen, *J. Mol. Struct.*, 2022, **1264**, 133258.
86 Y. Ma, A. Y. Chen, X. F. Xie, X. Y. Wang, D. Wang, P. Wang, H. J. Li, J. H. Yang and Y. Li, *Talanta*, 2019, **196**, 563–571.
87 F. Gudarzy, A. B. Moghaddam, S. Mozaffari, Y. Ganjkhanlou, M. Kazemzad, R. Zahed and F. Bani, *Microchim. Acta*, 2013, **180**, 1257–1262.
88 G. Mi, M. Yang, C. Wang, B. Zhang, X. Hu, H. Hao and J. Fan, *Spectrochim. Acta, Part A*, 2021, **253**, 119555.
89 Q. Zhou, Y. Fang, J. Li, D. Hong, P. Zhu, S. Chen and K. Tan, *Talanta*, 2021, **222**, 121548.
90 P. Sivakumar, S. Priyatharshni and K. Kumar, *Mater. Chem. Phys.*, 2020, **240**, 122167.
91 J. Zhao, L. Huang, C. Sun, D. Zhao and H. Tang, *Food Chem.*, 2020, **323**, 126807.
92 S. M. Ghani, B. Rezaei, H. R. Jamei and A. A. Ensafi, *Anal. Bioanal. Chem.*, 2021, **413**, 377–387.
93 Z. Liu, P. Yin, H. Gong, P. Li, X. Wang and Y. He, *J. Lumin.*, 2012, **132**, 2484–2488.
94 N. Kalčec, N. Peranić, R. Barbir, C. R. Hall, T. A. Smith, M. A. Sani, R. Frkanec, F. Separovic and I. Vinković Vrček, *Spectrochim. Acta, Part A*, 2022, **268**, 120707.
95 C. Wang, H. Shi, M. Yang, Z. Yao, B. Zhang, E. Liu, X. Hu, W. Xue and J. Fan, *Colloids Surf., B*, 2021, **205**, 111874.
96 A. Moslehipour, A. Bigdeli, F. Ghasemi and M. R. Hormozi-Nezhad, *Microchem. J.*, 2019, **148**, 591–596.

97 J. Jana, J. S. Chung and S. H. Hur, *ACS Omega*, 2019, **4**, 17031–17038.
98 M. Chatterjee, P. Nath, S. Kadian, A. Kumar, V. Kumar, P. Roy, G. Manik and S. Satapathi, *Sci. Rep.*, 2022, **12**, 9061.
99 Z. Pourghobadi, P. Mirahmadpour and H. Zare, *Opt. Mater.*, 2018, **84**, 757–762.
100 J. Tang, Y. Su, D. Deng, L. Zhang, N. Yang and Y. Lv, *Analyst*, 2016, **141**, 5366–5373.
101 D. Kumar, S. Umrao, H. Mishra, R. R. Srivastava, M. Srivastava, A. Srivastava and S. Srivastava, *Sens. Actuators, B*, 2017, **247**, 170–178.
102 J. Lian, Y. He, N. Li, P. Liu, Z. Liu and Q. Liu, *Am. Chem. Soc.*, 2021, **60**, 1893–1901.
103 C. Bendicho, I. Lavilla, F. Pena-Pereira, I. d. la Calle and V. Romero, *Sens*, 2021, **21**, 7571.
104 X. Zhang, Y. Zhu, X. Li, X. Guo, B. Zhang, X. Jia and B. Dai, *Anal. Chim. Acta*, 2016, **944**, 51–56.